Brookite TiO$_2$ Nanorods as Promising Electrochromic and Energy Storage Materials for Smart Windows

Congcong Xing, Linlin Yang, Ren He, Maria Chiara Spadaro, Yu Zhang,* Jordi Arbiol, Junshan Li, Bed Poudel, Amin Nozariasbmarz, Wenjie Li, Khak Ho Lim, Yu Liu, Jordi Llorca, and Andreu Cabot*

Electrochromic smart windows (ESWs) offer an attractive option for regulating indoor lighting conditions. Electrochromic materials based on ion insertion/desertion mechanisms also present the possibility for energy storage, thereby increasing overall energy efficiency and adding value to the system. However, current electrochromic electrodes suffer from performance degradation, long response time, and low coloration efficiency. This work aims to produce defect-engineered brookite titanium dioxide (TiO$_2$) nanorods (NRs) with different lengths and investigate their electrochromic performance as potential energy storage materials. The controllable synthesis of TiO$_2$ NRs with inherent defects, along with smaller impedance and higher carrier concentrations, significantly enhances their electrochromic performance, including improved resistance to degradation, shorter response times, and enhanced coloration efficiency. The electrochromic performance of TiO$_2$ NRs, particularly longer ones, is characterized by fast switching speeds (20 s for coloration and 12 s for bleaching), high coloration efficiency (84.96 cm^2 C^{-1} at a 600 nm wavelength), and good stability, highlighting their potential for advanced electrochromic smart window applications based on Li$^+$ ion intercalation.

1. Introduction

Electrochromism is a phenomenon where a material's optical properties, such as color or transparency, can be changed by applying an electric current.[1,2] This phenomenon is generally related to structural changes, chemical reduction/oxidation processes, and/or intercalation of extrinsic ions.[3,4] This reversible process makes electrochromic materials attract increasing interest in various applications, including smart windows, displays, and sensors.[5,6] The importance of electrochromism lies in its ability to provide energy-efficient solutions for controlling the amount of light and heat that enter a building.[7,8] For instance, smart windows made with electrochromic materials can switch from transparent to opaque or tinted to reduce the amount of solar heat gain, thereby improving the energy efficiency of buildings and

C. Xing, Y. Zhang, B. Poudel, A. Nozariasbmarz, W. Li
Department of Materials Science and Engineering
Pennsylvania State University
University Park, PA 16802, USA
E-mail: yvz5897@psu.edu

C. Xing, L. Yang, R. He, Y. Zhang, A. Cabot
Catalonia Institute for Energy Research (IREC)
Sant Adrià de Besòs
Barcelona 08930, Spain
E-mail: acabot@irec.cat

C. Xing, J. Llorca
Institute of Energy Technologies
Department of Chemical Engineering and Barcelona Research Center in Multiscale Science and Engineering
Universitat Politècnica de Catalunya
EEBE, Barcelona 08019, Spain

L. Yang, R. He
Departament d'Enginyeria Electronica i Biomedica
Universitat de Barcelona
Barcelona 08028, Spain

M. C. Spadaro, J. Arbiol
Catalan Institute of Nanoscience and Nanotechnology (ICN2)
CSIC and BIST
Campus UAB
Bellaterra, Barcelona 08193, Spain

J. Arbiol, A. Cabot
ICREA
Pg. Lluis Companys 23
Barcelona 08010, Spain

J. Li
Institute for Advanced Study
Chengdu University
Chengdu, Sichuan 610106, China

K. H. Lim
Institute of Zhejiang University-Quzhou
Quzhou, Zhejiang 324000, China

Y. Liu
School of Chemistry and Chemical Engineering
Hefei University of Technology
Hefei, Anhui 230009, China

reducing energy costs. Electrochromic materials also find applications in automotive rearview mirrors that automatically dim in response to headlights, aircraft windows that can change tint to reduce glare and heat, and displays that can change color or brightness based on user preferences or environmental conditions.[9,10] Thus, electrochromism offers the appealing potential to provide energy-efficient and cost-effective solutions for a variety of applications that require dynamic control of optical properties.

Various metal oxides and conducting polymers have been investigated as promising electrochromic materials.[11–14] Inorganic electrochromic materials, such as titanium oxide,[15,16] tungsten oxide,[17,18] niobium oxide,[19,20] nickel oxide,[21,22] and molybdenum oxide,[23,24] have better commercial prospects due to their excellent thermal and chemical stability, abundance of their constituent elements, low cost, safety, and notable performance. Among these inorganic electrochromic materials, TiO_2 stands out as an especially promising candidate. Within the TiO_2 lattice, the Ti^{4+} ions are surrounded by six O^{2-} ions to create an $[TiO_6]$ octahedron, forming large vacant sites that provide enough space for the accommodation of protons or other guest ions.[25] Within electrochromic smart windows (ESWs), the coloration mechanism of TiO_2 is generally related to the insertion or extraction of Li^+ from the ion-conducting electrolyte into the TiO_2 lattice accompanied by the reduction of TiO_2.[26,27]

$$TiO_2 + xLi^+ \leftrightarrow Li_xTiO_2 \qquad (1)$$

Despite the coloration mechanism remaining the same, the electrochromic properties of TiO_2 have been demonstrated to be influenced by its crystallographic phase,[28] electronic conductivity,[29] and defect level.[27,30] While considerable research efforts have been devoted to the development of TiO_2-based ESWs, key parameters such as the TiO_2 particle size and morphology have been rarely investigated. The brookite phase of TiO_2 outperforms the anatase and rutile phases, displaying superior performance in electrochromism, dielectrics, photoactivity, catalytic activity, and electrochemistry,[31–33] attributed to its distinct structural characteristics, including a distorted lattice and variable Ti–O bond lengths.[34]

In addition to composition and crystal structure, the material architecture, including particle shape, morphology, and arrangement, plays a pivotal role in determining optical and electrochemical performance.[35–41] TiO_2 nanoparticles, nanoflakes, and amorphous/crystalline structures exhibit excellent electrochromic performance due to their unique properties.[42–46] Among them, 1D materials such as nanorods (NRs) and nanowires offer several advantages in ESWs. First, 1D materials have a large specific surface area that allows for efficient interaction with the electrolyte while simultaneously facilitating charge transport, which reduces charge-transfer resistance.[47] Second, 1D materials are highly tolerant to volume changes during ion insertion/extraction, which minimizes damage to the electrode structure and improves stability.[48] Third, electrodes based on 1D materials promote ion diffusion and enhance contact between the electrolyte and electrode, thereby shortening the charge and discharge time threshold and the distance of electron transport and ion diffusion.[20] For instance, Chen et al.[49] demonstrated that anatase TiO_2 nanowire electrodes improve the optical

transparency in ESWs. Similarly, Chen et al.[50] reported that core-shell NR arrays of crystalline/amorphous TiO_2 enhance electrochromic performance.

We synthesized TiO_2 NRs with tunable lengths using a colloidal approach and investigated their performance as electrochromic materials. We analyzed the importance of optimizing the length of TiO_2 NRs to achieve optimal electrochromic performance. The inherent defects in the NRs contribute to efficient Li^+ insertion/extraction and enhance electrochromic response efficiency. The TiO_2 NRs demonstrate reduced impedance, facilitating faster charge transport and ion diffusion, resulting in shorter response times and improved color-switching capabilities. Subsequently, we used them to assemble ESW devices. The electrochromic properties of the TiO_2 NR-based ESW devices were further evaluated, including coloration and bleaching rates, coloration efficiency, and stability, which sheds light on the mechanism of electrochromic performance and provides a pathway toward developing more efficient and reliable ESW devices for energy storage applications.

2. Results and Discussion

Colloidal TiO_2 NRs were synthesized via a hydrolysis approach in an organic solution (see details in the Experimental section). In brief, titania nuclei were produced in the presence of oleylamine (OAm), 1-octadecanol (ODO), oleic acid (OAc), and eventually 1,2-hexadecanediol (HDDOL) or methylamine hydrochloride (MAC), by heating to 290 °C a titanium (IV) chloride ($TiCl_4$) precursor stock solution obtained by dissolving $TiCl_4$ in OAc and ODO. At this moderate temperature, OAm and OAc slowly react to generate small amounts of water, resulting in slow hydrolysis and condensation of $TiCl_4$ along with the release of HCl. After nucleation, TiO_2 NRs were further grown by slowly adding additional amounts of the $TiCl_4$ stock solution into the initial nuclei solution maintained at 290 °C. This two-step synthesis approach allows for preventing the nucleation of additional NRs during the growth of the preformed ones. As shown in Figure S1, Supporting Information, the initially formed nuclei in the absence of HDDOL or MAC already presented elongated morphologies with an average length of 15 ± 5 nm. After the nucleation step, simultaneous and uniform growth of all the nuclei in the ensemble takes place and the TiO_2 particles preserve the NR morphology, a relatively narrow size distribution, and excellent colloidal stability (**Figure 1**a–c).

Transmission electron microscopy (TEM) characterization showed that when adding no HDDOL and no MAC, TiO_2 NRs with an average length of 30 ± 12 nm and an average thickness of 2.6 ± 0.6 nm were obtained (Figure 1b and Figure S2, Supporting Information). This sample will be referred to as M-TiO_2, standing for medium TiO_2. In the presence of a small amount of HDDOL in the initial solvent solution, shorter TiO_2 NRs, with an average length of 17 ± 5 nm and an average thickness of 2.5 ± 0.7 nm, were produced (Figure 1a and Figure S2, Supporting Information). This sample will be referred to as S-TiO_2, standing for short TiO_2. In contrast, when adding a small amount of MAC, longer TiO_2 NRs, with an average length of 45 ± 16 nm and an average thickness of 2.8 ± 0.8 nm, were grown (Figure 1c and Figure S2, Supporting Information). This sample will be referred to as L-TiO_2, standing for long TiO_2. High-resolution TEM (HRTEM)

ADVANCED
SCIENCE NEWS
www.advancedsciencenews.com
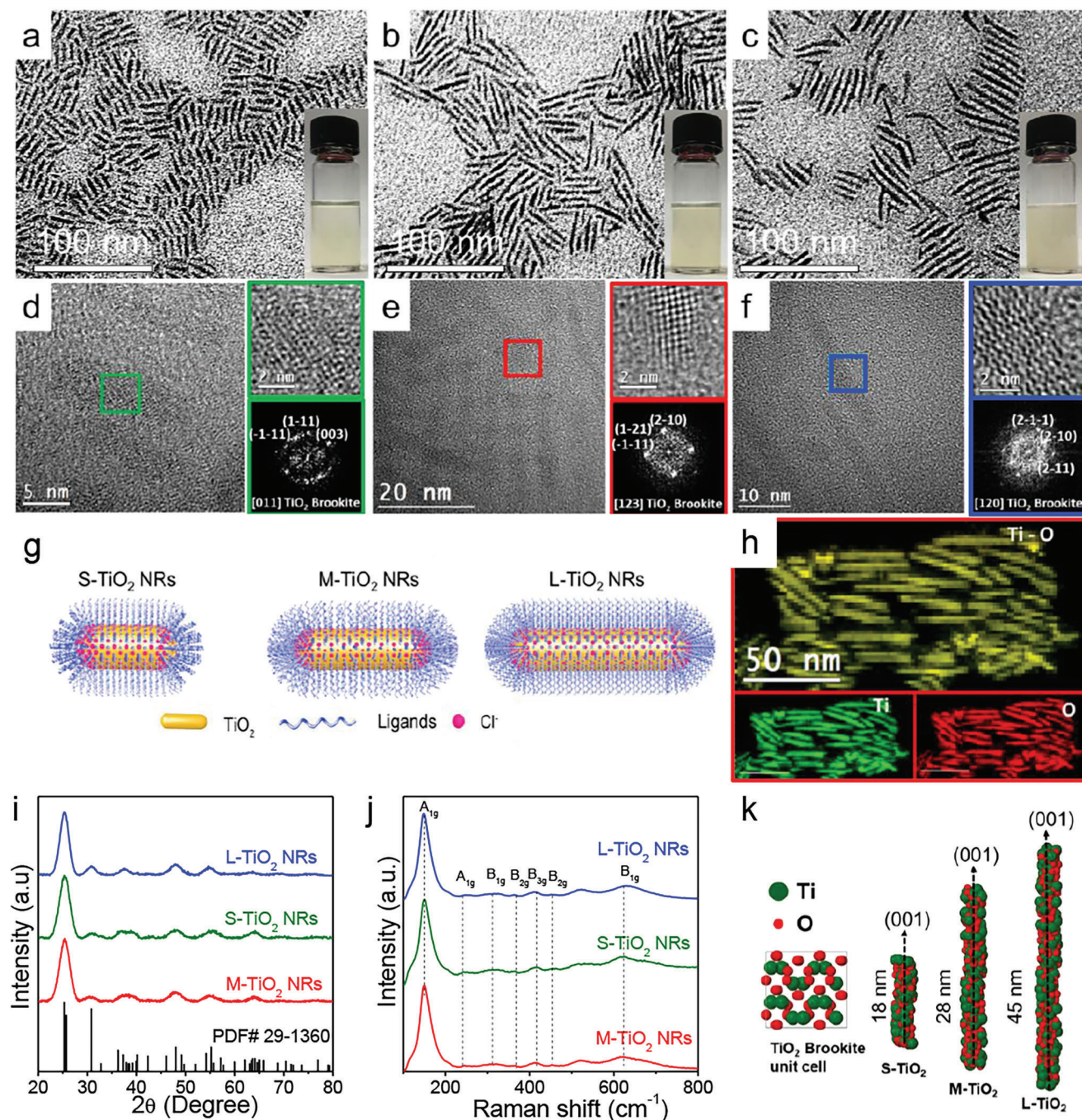
NANO · MICRO
small
www.small-journal.com

Figure 1. a–c) Representative TEM micrographs and optical images of S, M, and L-TiO$_2$ dispersed in hexane solution with a concentration of 10 mg mL^{-1}. d–f) HRTEM micrographs of TiO$_2$ NRs showing the Brookite orthorhombic crystal phase: d) S-TiO$_2$ NRs oriented along the [011] zone axis; e) M-TiO$_2$ NRs oriented along the [123] zone axis; f) L-TiO$_2$ NRs oriented along the [120] zone axis. g) Schematic illustration of the influence of HDDOL and MAC on the size and aspect ratio of the TiO$_2$ NRs. h) EELS chemical composition maps of L-TiO$_2$ NRs: Ti L edge at 456 eV (green) and O K edge at 532 eV (red). i) Powder XRD patterns (reference pattern for brookite TiO$_2$ JCPDF No. 29–1360), j) Raman spectra, and k) 3D atomic models of S, M, and L-TiO$_2$ NRs.

analyses of the different TiO$_2$ NRs (Figure 1d–f) showed them to be characterized by the brookite orthorhombic crystal structure. Table S1, Supporting Information, summarizes the main geometry characteristics of the synthesized TiO$_2$ NRs with different lengths. As shown in Figure 1h, electron energy loss spectroscopy

(EELS) elemental maps of the TiO$_2$ NRs recorded at the Ti L edge at 456 eV and O K edge at 532 eV display a homogeneous distribution of Ti and O within the nanostructures.

Both the thermodynamics of the system and the kinetics of the nucleation and growth process can determine the morphology

**ADVANCED
SCIENCE NEWS**

www.advancedsciencenews.com

NANO · MICRO

small

www.small-journal.com

of the final structure. Specifically, thermodynamic properties[51] determine that brookite TiO$_2$ only exists as nanocrystalline particles and that the stability of both anatase and brookite is closely related to the particle size, being the brookite phase more stable in the range of 10–40 nm. For brookite TiO$_2$ nanocrystals, the [001] crystal facets have high energy.[52,53] Thus, energy is minimized by growing preferentially along the [001] direction, especially in the presence of chlorine ions (Cl$^-$).[54,55]

The routes toward TiO$_2$ NRs with different aspect ratio is shown in Figure 1g. While OAm and OAc play a double role as coordinating/stabilizing solvents and releasing water, Cl$^-$ is key in directing the TiO$_2$ asymmetric growth and determining its aspect ratio. MAC and HDDOL were introduced to tune the amount of chlorine binding at the nanoparticle surface. We hypothesize that while the introduction of hydrochloride increases the chlorine concentration, the presence of the diol competes with chloride for the binding at the TiO$_2$ NR surface, decreasing the surface concentration of chlorine. Since the thickness of all the NRs is approximately the same and the volume of TiO$_2$ grown must be similar for all the samples, the difference in lengths must come from a different number of NRs, i.e. from the amount of NR nuclei initially produced within each ensemble. Thus, we conclude that the presence of HDDOL, reducing the amount of surface Cl$^-$, promotes the TiO$_2$ nucleation, while the presence of MAC, increasing the amount of capping Cl$^-$, hampers it.

The formation of the brookite phase was confirmed by X-ray diffraction (XRD) and Raman spectroscopy. The sharp XRD diffraction peaks of each sample match well with the standard diffraction pattern of brookite (JCPDF No. 29–1360), with no additional XRD peak detected (Figure 1i). Besides, the main characteristic peaks of anatase that do not overlap with brookite, at 2θ of 62.57° and 75.0°, are not observed, pointing to a pure brookite phase (Figure S3, Supporting Information). The significant difference in XRD peak intensity further confirms the asymmetric geometry of the crystalline domains.[56]

Raman spectroscopy was further used to confirm the crystalline structure of TiO$_2$ (Figure 1j). The Raman spectra of the TiO$_2$ NRs display several Raman peaks attributed to the brookite TiO$_2$ Raman vibration modes at A$_{1g}$ (152 and 246 cm^{-1}), B$_{1g}$ (327 and 622 cm^{-1}), B$_{2g}$ (366 and 460 cm^{-1}), and B$_{3g}$ (416 cm^{-1}).[57] Thus, the Raman spectra of the TiO$_2$ NRs are also in good agreement with the brookite crystal phase. Overall, according to the TEM, HRTEM, XRD, and Raman results shown above, the 3D models of the TiO$_2$ brookite NRs are displayed in Figure 1k.

Figure S4, Supporting Information, depicts the electron paramagnetic resonance (EPR) spectra measured at 77 K of TiO$_2$ NRs with various lengths. EPR spectra exhibit distinct characteristics associated with lattice and surface Ti^{3+} vacancy centers for S, M, and L-TiO$_2$ NRs. Notably, the EPR signal intensity of L-TiO$_2$ NRs is significantly higher than that of S-TiO$_2$ and M-TiO$_2$ NRs, indicating that longer TiO$_2$ NRs possess a higher defect density. Furthermore, high-resolution X-ray photoelectron spectroscopy (XPS) spectra revealed a shoulder in the Ti 2p spectrum, indicating the presence of Ti^{3+} within the TiO$_2$ lattice, along with a positive shift in both the Ti 2p and O 1s spectra indirectly related

to the presence of abundant defects that can shift upwards the Fermi level (Figure S5, Supporting Information).[58]

For the preparation of an optically transparent electrochromic thin film electrode, a layer of TiO$_2$ NRs with a thickness of ≈2 μm was spin-coated on an indium-doped tin oxide (ITO)-coated glass (Figure S6b, Supporting Information). The films were afterward heated in the air at 350 °C for 45 min to remove the organic ligands. The in situ UV–vis optical transmittance spectra versus $E_{Ag/AgCl}$ potential from −4 to 0 V of S, M, and L-TiO$_2$ NRs thin films were first investigated in view of their use as a cathodic electrochromic electrode for ESWs (**Figure 2**a–c). XRD analysis confirms that the brookite phase is preserved (Figure S7, Supporting Information) after heat treatment. TEM analysis (Figure S8a–f, Supporting Information) reveals a significant aggregation of the TiO$_2$ NRs during deposition and annealing but with no impact on their geometry and size. Besides, annealing promotes a strong adhesion between TiO$_2$ NRs and ITO substrate and results in enhanced color modulation (Figure S8g,h, Supporting Information).

The optical modulation (ΔT) at different wavelengths of S, M, and L-TiO$_2$ NRs thin films was calculated using the following equation.

$$\Delta T = (T_b - T_c)/T_b \times 100\% \qquad (2)$$

where T_c represents the transmittance of the device in the colored state, and T_b represents the transmittance in the bleached state. As shown in Figure 2d, the L-TiO$_2$ electrode exhibited the highest ΔT values compared to the M and S-TiO$_2$ electrodes, particularly at the wavelengths of 400, 600, and 800 nm. Additionally, the L-TiO$_2$ electrode required the lowest applied potential to achieve the same transmittance as the other TiO$_2$ NR-based electrodes. The optical photographs in Figure 2e demonstrate that increasing the applied potential to the TiO$_2$ NRs on the ITO glass resulted in a gradual decrease in transmittance intensity. To evaluate the reproducibility of the L-TiO$_2$ NRs thin film device, a series of four samples were fabricated using the same process and underwent in situ UV–vis optical transmittance measurements (Figure S9, Supporting Information). The results demonstrated remarkable consistency in performance across all the fabricated samples. Furthermore, additional measurements were carried out at different temperatures, shedding light on the temperature-dependent behavior of the devices. Notably, the data presented in Figure S10, Supporting Information, clearly illustrates that temperatures above 35 °C have a detrimental effect on both the performance and stability of the devices. These findings provide crucial insights into the operational limitations and thermal stability considerations associated with TiO$_2$ thin film devices.

Electrochemical impedance spectroscopy (EIS) spectra were obtained in 1M LiClO$_4$ within propylene carbonate (PC) electrolyte to investigate the charge transfer of the TiO$_2$ thin films. The Nyquist plots of the EIS spectra obtained from S, M, and L-TiO$_2$ electrodes are shown in Figure 2f. The serial resistance (R_s), charge-transfer resistance (R_{ct}), and capacitance of the double-layer capacitor (C_{dl}) were determined by fitting the Nyquist plots with an equivalent circuit model (see inset in Figure 2f) and are compiled in Table S2, Supporting Information. R_{ct} decreased with the NR length from
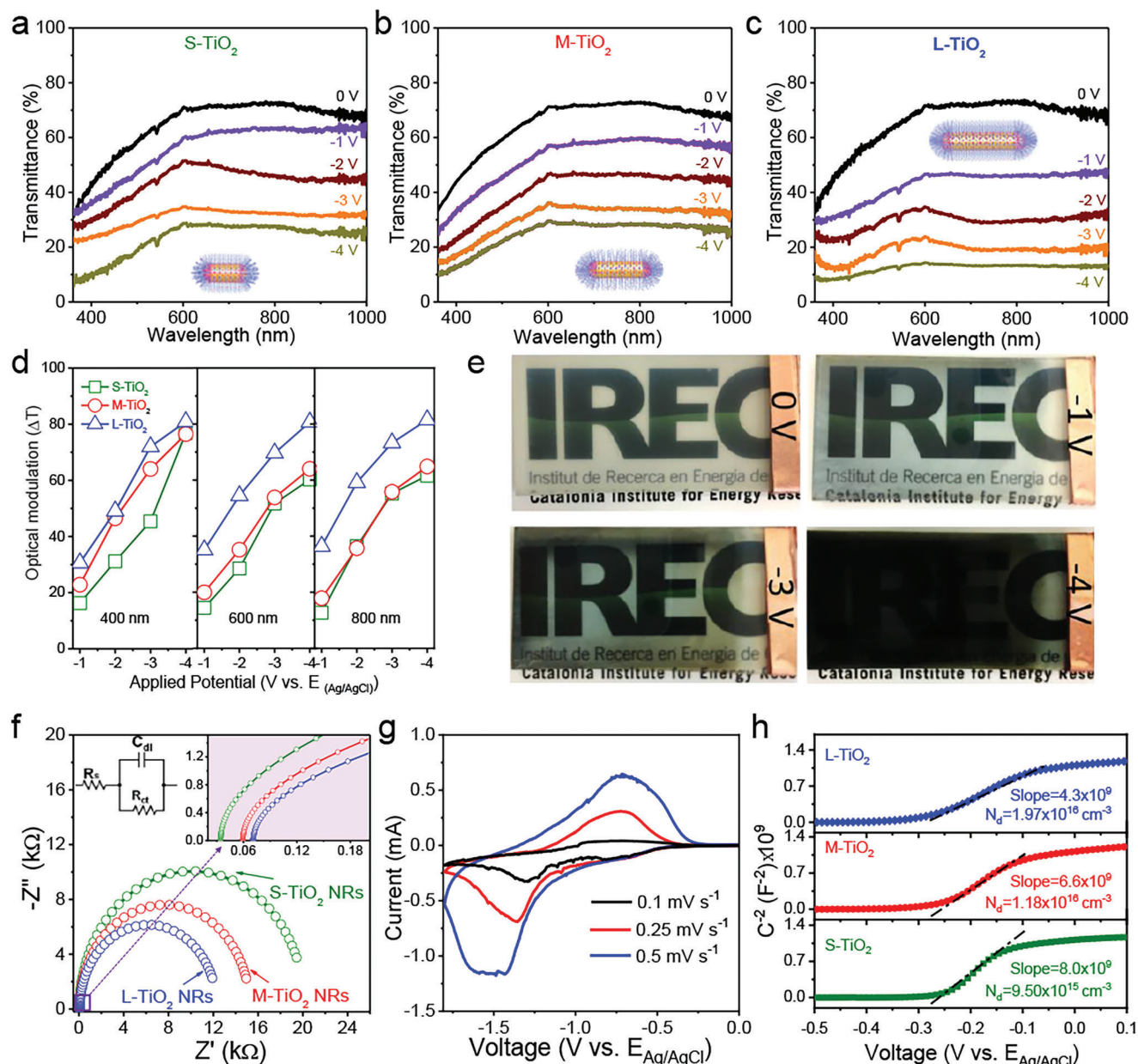
ADVANCED
SCIENCE NEWS
www.advancedsciencenews.com

NANO · MICRO
small
www.small-journal.com

Figure 2. a–c) In situ UV–vis optical transmittance spectra, d) the optical modulation (ΔT) at the wavelength of 400, 600, and 800 nm, and e) the optical photographs of L-TiO$_2$ NRs thin film electrodes with different applied potentials. f) Nyquist plots of S, M, and L-TiO$_2$ thin film electrode at 0.5 V versus $E_{Ag/AgCl}$; inset is the equivalent circuit model. g) CV curves of L-TiO$_2$ thin film electrode with scan rates of 0.1, 0.25, and 0.5 mV·s^{-1}; h) Mott–Schottky curves of S, M, and L-TiO$_2$ NRs.

20.1 kΩ for S-TiO$_2$ to 12.3 kΩ for L-TiO$_2$, demonstrating a faster charge-transfer process for the L-TiO$_2$. In contrast, C_{dl} remained constant and the serial resistance surprisingly increased with the NR length, which we associate with the differences in the film architecture related to the worse piling of the longer NRs. The smaller impedance in L-TiO$_2$ NRs indicates improved charge transport and better ion diffusion due to increased defect density, leading to faster response times and more efficient color change in electrochromic processes.

The cyclic voltammogram (CV) curves of L-TiO$_2$ films are displayed in Figure 2g. A pair of redox peaks are observed in each

CV curve obtained at different scan rates. The absolute ratio of the cathodic peak current ($i_{Pc} = -1.16 \times 10^{-3}$ A) and the anodic peak current ($i_{Pa} = 0.64 \times 10^{-3}$ A) is 2.1, implying reversibility. In electrochromic systems, the observed difference in peak currents, with higher cathodic peak current compared to anodic peak current, is primarily attributed to factors such as higher concentration of electroactive species and various kinetic and transport limitations affecting the reduction and oxidation reactions. Mott–Schottky (M–S) curves (Figure 2h) were used to analyze the carrier concentrations of three samples. The M–S curves were generated by measuring the capacitance as a function of applied

voltage, with the linear region representing the semiconductor behavior. The carrier concentrations (N_d) were calculated using the following formula.[59]

$$\frac{1}{C^2} = \frac{2}{\varepsilon \varepsilon_0 A^2 e N_d} \left(V - E_{fb} - \frac{K_B T}{e} \right) \qquad (3)$$

where A is the interphase area which is calculated from the geometric area of the NRs contained within the 1×2 cm^2 electrode, ε is 48, the dielectric constant of the TiO$_2$, ε_0 is the permittivity of free space, K_B is Boltzmann's constant, T is the absolute temperature, and e is the electronic charge. The carrier concentrations were determined to be 1.97×10^{16} cm^{-3} for L-TiO$_2$ NRs, 1.18×10^{16} cm^{-3} for M-TiO$_2$ NRs, and 9.50×10^{15} cm^{-3} for S-TiO$_2$ NRs, respectively, based on the analysis of the M-S curves (Figure 2h). The results indicate an increasing trend in carrier concentration, with a slightly higher density of charge carriers in L-TiO$_2$ NRs. These differences in charge carrier concentration between the different TiO$_2$ NRs should be attributed to the different defect levels, as observed by EPR and XPS analysis, but may be in part modulated by the underlying ITO.

The L-TiO$_2$ NRs exhibit a significant defect density on their surface, as observed by XPS and EPR analysis. This abundance of defects provides numerous active sites for redox reactions, resulting in remarkable electrochromic activity and coloration efficiency. Moreover, the L-TiO$_2$ NRs demonstrate lower impedance and higher carrier concentration, indicating enhanced charge transport and Li$^+$ diffusion within the material. As a result, electrochromic devices incorporating L-TiO$_2$ NRs exhibit faster response times and more efficient color switching. The combination of higher defect density, reduced impedance, and increased carrier concentration collectively contributes to the exceptional electrochromic performance of the L-TiO$_2$ NRs, positioning them as highly promising materials for advanced electrochromic applications.

The architecture of an ESW device is shown in **Figure 3**a. The ≈2 μm thick L-TiO$_2$ thin film on ITO glass outperformed TiO$_2$ films of 1 and 4 μm thicknesses, demonstrating the most favorable performance under identical applied voltage conditions (Figure S6, Supporting Information), with a ≈2 μm-thick NiLi$_{0.83}$Ti$_{0.28}$O$_x$ anodic electrochromic electrode in 1 M LiClO$_4$/PC electrolyte. To evaluate the switching performance of the assembled ESW device, the in situ current density and transmittance at 600 nm were monitored by combining an electrochemical workstation and a UV–vis spectrophotometer, and switching the voltage using a square-wave function between 1 and −3 V versus $E_{Ag/AgCl}$. Figure 3b shows the current density and transmittance transients upon switching the applied potential. The ESW device shows good switching and electrochromism properties and a constant ΔT during these cycles (Figure S11, Supporting Information). Besides, the coloration response time was evaluated through double potential-step chronoamperometry (−4 and 0 V) measurement. The coloration and bleaching response time of ESWs is defined as the time it takes for a 90% change between the colored and bleached states. For ESWs based on L-TiO$_2$, the coloration time ($t_{c,90\%}$) was calculated to be 20 s, while the bleaching time ($t_{b,90\%}$) was determined to be 12 s, which benefit from the fast charge transfer and low R_{ct} of the L-TiO$_2$ thin film (Figure 3c). Faster electrochemical reaction during

charging leads to shorter coloration time in electrochromic devices compared to the bleaching time during discharging. The fast response with a low voltage of the L-TiO$_2$ thin films is expected to mitigate the challenge in large voltage requirements across the large-area ESW devices. To evaluate the ESW performance, coloration efficiency (CE) is calculated according to Equation (4).[60]

$$CE = \Delta OD/\Delta Q = log\left(T_b/T_c\right)/\Delta Q \qquad (4)$$

where T_b and T_c are the transmittance intensity at a special wavelength in bleached and colored states, respectively; and ΔQ is the required charge density for the corresponding changed optical density (ΔOD). Thus, CE is calculated from the slope of the linear region of the ΔOD versus ΔQ plots (Figure S12, Supporting Information). The obtained CE is 84.96 cm^2 C^{-1} for the L-TiO$_2$ NRs at 600 nm, which is higher than other reported TiO$_2$-based electrochromic electrodes (Table S3, Supporting Information).[31,50,27,61,62]

The optical transmittance spectra of the L-TiO$_2$ thin film under three applied potentials (0, −2.5, and −4 V) are depicted in Figure 3d. The results demonstrate effective control over visible (vis) and near-infrared (NIR) light transmittance intensity by adjusting the applied potentials. At 0 V, the TiO$_2$ thin film appears colorless and exhibits complete transparency to both vis and NIR spectra (400–1000 nm), referred to as the transparent mode. This mode is ideal for applications requiring high visible light transmission and daylighting displays. At −2.5 V, the L-TiO$_2$ thin film blocks 60.2% of vis and NIR light transmittance intensity, representing the cloudy mode. When the applied potential is set to −4 V, the TiO$_2$ thin film shows significantly reduced vis and NIR light transmittance intensity (17.5%). The black mode is suitable for applications that prioritize personal privacy protection and reduction of solar heat gain in buildings. Digital photos of the TiO$_2$ thin film electrode in the transparent, cloudy, and black modes are presented in Figure 3e.

The switching mechanism between these modes is based on Li$^+$ intercalation within the TiO$_2$ thin film electrode. A schematic illustration of the ESW device in the three modes is depicted in Figure 3f–h. With no applied potential, the TiO$_2$ thin film just adsorbs Li$^+$ on its surface, with no intercalation, which corresponds to the transparent mode (Figure 3f). At a moderate applied potential of −2.5 V, a moderate Li$^+$ is inserted into the TiO$_2$ crystal lattice to induce the partial LiTiO$_x$ transformation, thus leading to a moderate blocking of the light, which corresponds to the cloudy mode. (Figure 3g). With a further increase in the applied potential to −4 V, more Li$^+$ is inserted into the TiO$_2$ lattice, forming the Li$_x$TiO$_2$ phase which has a high absorption in the UV–vis, thus it is referred to as the black mode (Figure 3h) and alters the transmittance of both vis and NIR light.

To investigate the long-term stability of the assembled ESW device, the optical transmittance spectra of the L-TiO$_2$ thin film electrode before and after 500 full switching cycles, that is, up to −4 V, are shown in **Figure 4**a. The ΔT of L-TiO$_2$ thin film electrode at 400, 600, and 800 nm with an applied potential at −2.5 and −4 V is summarized in Figure S13, Supporting Information. 96.1– 99.2% of the ΔT is maintained after 500 full cycles of the L-TiO$_2$ thin film electrode, implying good coloration

**ADVANCED
SCIENCE NEWS**

www.advancedsciencenews.com

NANO · MICRO
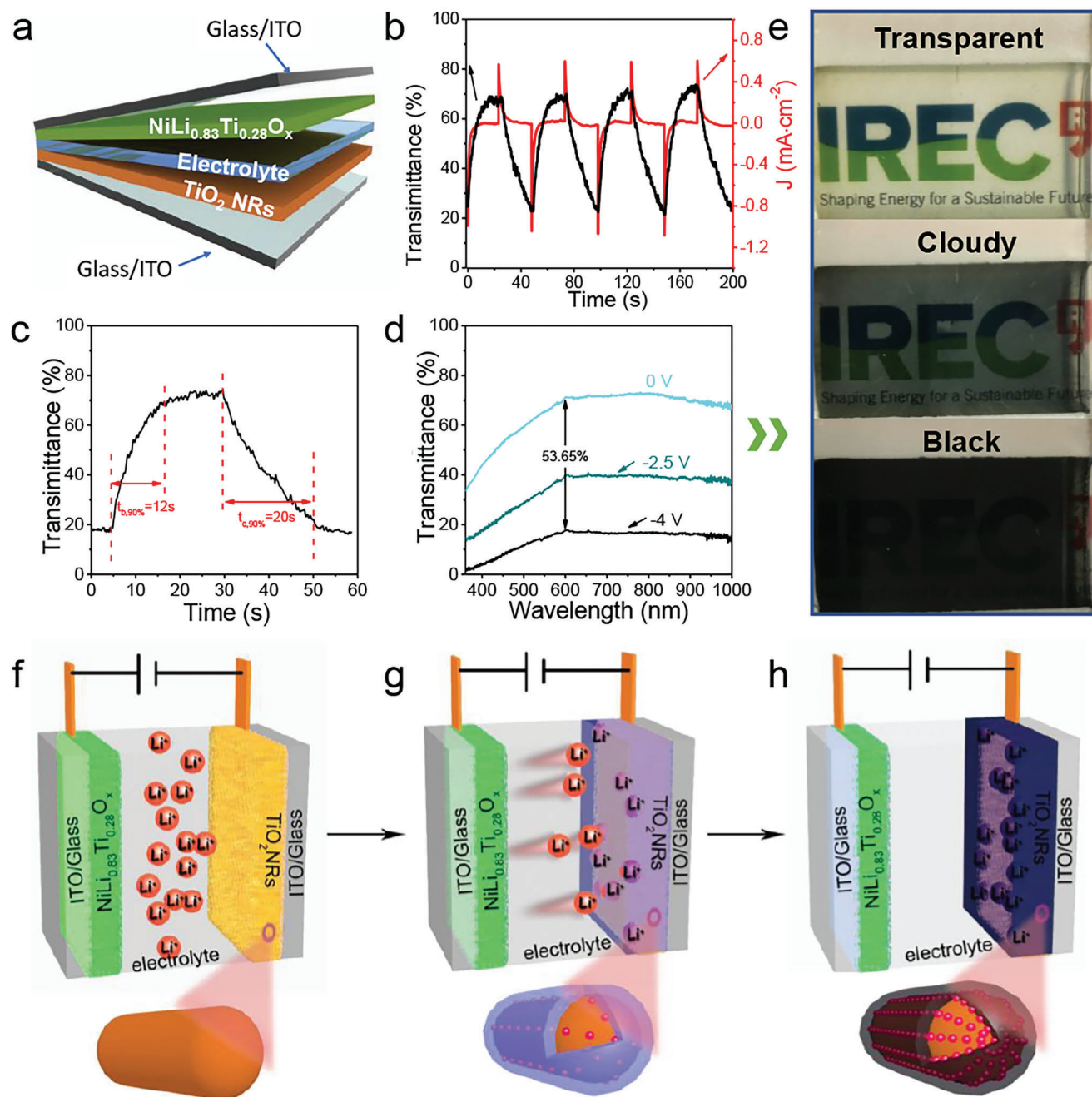
small

www.small-journal.com

Figure 3. a) Schematic illustration of the ESW device structure with the sandwich structure of $ITO/TiO_2/electrolyte/NiLi_{0.83}Ti_{0.28}O_x/ITO$. b) Transmittance at 600 nm wavelength and current density (J) of the ESW device upon electrochromic switching with a potential of 1 and -3 V with a cycle time of 50 s. c) Change of transmittance of the ESW device at 600 nm upon a switching cycle with a potential of 0 and -4 V with time intervals of 80 s. d) Transmittance spectra from 300–1000 nm of the L-TiO_2 thin film under three potential set values of 0, -2.5, and -4 V. e) Optical photographs of the ESW device at the corresponding "transparent", "cloudy" and "black" modes. f–h) Schematic illustration of the ESW device in three modes during Li^+ insertion.

stability, attributed to the TiO_2 1D NR structure with high tolerance to electrode volume changes during the Li^+ intercalation, which is higher than other reported TiO_2-based electrochromic electrodes.[27,62–64] The CV curves of the ESW device before and after the 200 switching cycles are shown in Figure S14, Supporting Information. Just a slight current decrease of the ESW device is observed after the 200th coloration cycle, further proving its good stability.

TiO_2-based ESW can store the energy used to change their transmittance mode, which allows for maximizing the energy efficiency of the process. ESW could be even potentially used as building integrated structural energy storage devices,
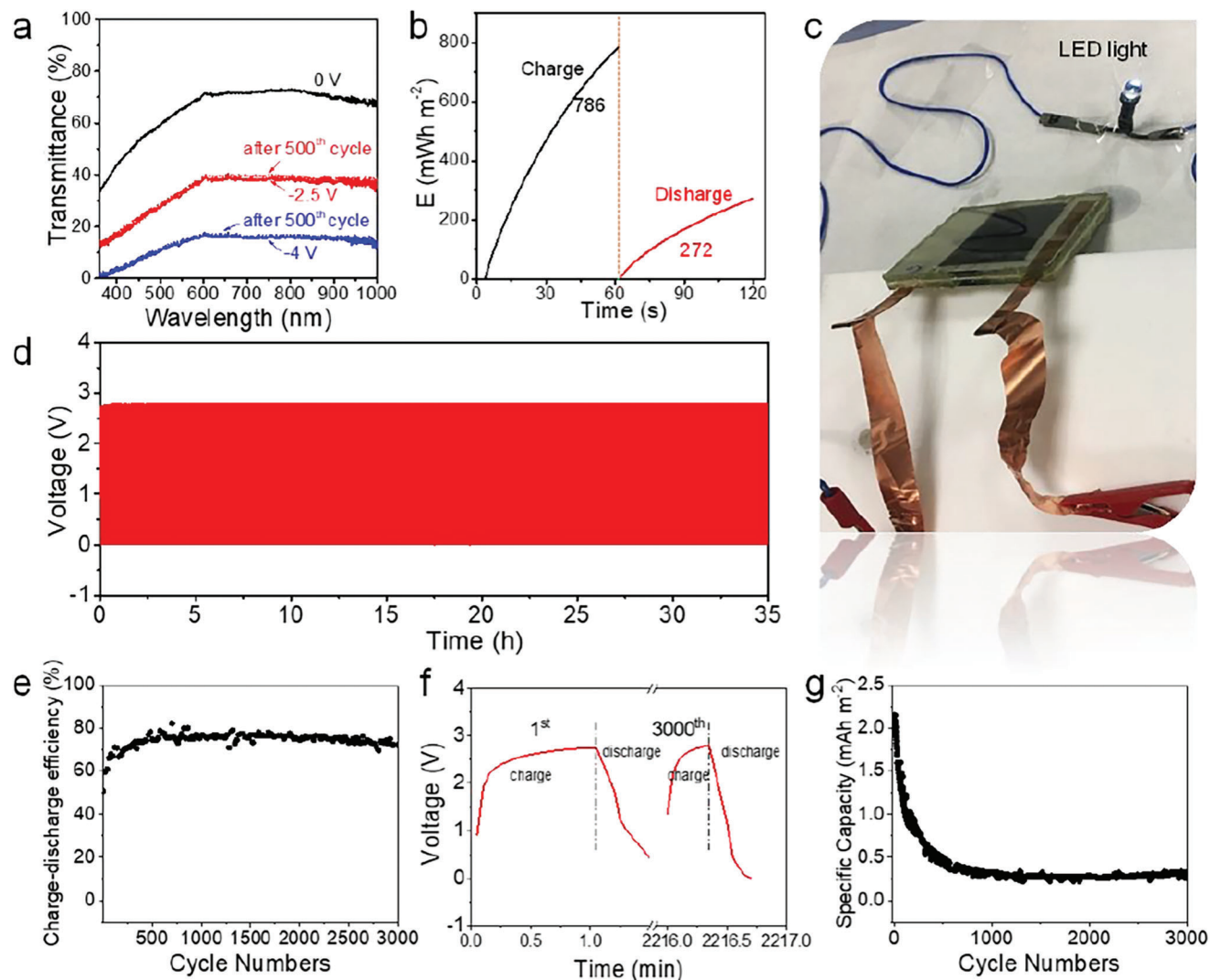
**ADVANCED
SCIENCE NEWS**

www.advancedsciencenews.com

**NANO · MICRO
small**

www.small-journal.com

Figure 4. a) Transmittance spectra of L-TiO$_2$ thin film electrode before and after the 500 switching cycles. b) Galvanostatic charge curve (black line) at a current density of −4 V for 60 s and potentiostatic discharge curve (red line) for 60 s. c) A photograph of a LED (2 V) lighted by an ESW device. d) Charge/discharge curves for the ESW device at a current of 0.2 mA with a charge threshold voltage of 2.8 V. The effective area of the ESW device is 2.5 × 4 cm^2. e) Charge-discharge efficiency of the ESW device. f) Charge/discharge curves for the ESW device at the 1st and 3000th cycles. g) Specific capacity for the ESW device at different cycles.

contributing to solving the current limitations in energy storage being part of the future energy storage mix.[65,66] As shown in Figure 4b, during the coloration process, the ESW device was charged potentiostatically at −4 V for 60 s with an energy consumption of 786 mWh m^{-2}. In the bleaching process, ESW was discharged from −4 V for 60 s recovering 272 mWh m^{-2}, which could light up an LED bulb for more than 30 s (Figure 4c and Video S1, Supporting Information).

Figure 4d shows extended charge/discharge curves, for 35 h and ≈3000 cycles, of the ESW device up to 2.8 V at a current of 0.2 mA. The size of the ESW device is 5 × 5 cm^2, and the effective area is 2.5 × 4 cm^2. Charge and discharge curves at a higher rate of 0.5 mA are displayed in Figure S15, Supporting Information. As shown in Figure 4e, the charge-discharge efficiency of the TiO$_2$ ESW device is above 50% at the first cycle and increases up to 75% at the 500th cycle when it stabilizes, proving its

long-time cycling stability and long lifetime. The initial improvement in charge-discharge efficiency of the TiO$_2$ NRs-based ESW device before 500 cycles is attributed to the activation and optimization of electrochemical processes and the formation of a stable solid-electrolyte interface. These findings highlight the favorable electrochemical properties of TiO$_2$ NRs for reliable ESW applications. As the charge and discharge cycles increase, the TiO$_2$-based ESW devices require less time to reach the threshold voltage, as shown in Figure 4f, implying a decrease in capacity. The longer charging time in TiO$_2$ NRs-based electrochromic devices compared to discharging can be attributed to factors such as slower redox reaction kinetics, limited ion diffusion during charging, and favorable material properties.[67,68] The initial specific capacity of the TiO$_2$-based ESW device reaches 2.1 mAh m^{-2}, which is the maximum charge that the device can store when it is fully charged. However, after 500 cycles, the specific capacity

**ADVANCED
SCIENCE NEWS**

www.advancedsciencenews.com

**NANO · MICRO
small**

www.small-journal.com

decreases to 0.5 mAh m^{-2}, indicating a decrease in the amount of charge, which could be ascribed to various factors, such as the degradation of the electrodes or the loss of active sites. The specific capacity further decreases to 0.3 mAh m^{-2} at the 1000th cycle, where it stabilizes and reaches a steady-state condition, and further degradation is unlikely. Figure 4g depicts the change in specific capacity over multiple cycles, which reveals the gradual decrease in specific capacity over time and the stabilization of the capacity after 1000 cycles.

3. Conclusion

In summary, TiO$_2$ NRs with tunable lengths ranging from 17–45 nm were produced using a colloidal synthesis method, and their performance as electrochromic materials were investigated. Optimizing the length of TiO$_2$ NRs is crucial for achieving optimal electrochromic performance. The longest NRs exhibit higher defect density, smaller impedance, and higher carrier concentration, resulting in superior electrochromic performance and promising applications. Using these longest NRs, we assembled electrochromic smart ESW devices and evaluated their electrochromic properties. The devices based on the longest TiO$_2$ NRs exhibited excellent electrochromic properties, including fast coloration and bleaching rates, high coloration efficiency, and good stability. Furthermore, we demonstrated three optical modes and unveiled the mechanism of the switching of these modes based on the intercalation within the TiO$_2$ lattice of Li$^+$ in the electrolyte. These findings offer insights into the TiO$_2$ NRs-based electrochromic performance mechanism and a pathway to design and engineering more efficient and reliable ESW devices for diverse optical display applications.

4. Experimental Section

Materials: TiCl$_4$, lithium perchlorate (LiClO$_4$, 99.99%), PC, anhydrous, 99.7%, nickel acetate tetrahydrate (Ni(CH$_3$COO)$_2$ 4H$_2$O, 98%), titanium isopropoxide (Ti(OC$_3$H$_7$)$_4$, 97%), lithium acetate (CH$_3$COOLi, 99.95%), and HDDOL, C$_{16}$H$_{34}$O$_2$, 90% were purchased from Fisher Scientific. 1-ODO (99%), OAC (90%), OAm (90%), and MAC (98%) were purchased from Sigma-Aldrich. All chemicals were used as received. ITO-coated glass slides (5 × 5 cm, 2.2 mm-thick, 6–9 Ω sq^{-1}) were supplied by Dyesol (TEC8 Glass).

Preparation of Stock Solutions: Stock solutions were prepared in a glovebox under a nitrogen atmosphere. The TiCl$_4$ stock solution consisted of 0.12 g TiCl$_4$ in 1.5 mL OAc and 3.4 mL 1-ODO. 1-ODO and OAc were purified by vacuum distillation. The TiCl$_4$ stock solution was stirred on a hot plate at a temperature of 80 °C to promote the dissolution of TiCl$_4$. Once dissolved, the TiCl$_4$ stock solution turned to be brown.

Synthesis of TiO$_2$ NRs: In a 100 mL flask, 15 mL OAm, 5.2 mL 1-ODO, 0.25 mL OAc, and (10 mmol of HDDOL for S-TiO$_2$ or MAC for L-TiO$_2$) were combined and degassed at 120 °C for 1 h. After degassing, the system was allowed to cool down to 60 °C to add 0.25 mL of the desired stock solution (or mixed stock solution). Then, the solution was quickly heated to 290 °C for 15 min and held for 10 min to allow for the formation of seed crystals. A 4 mL stock solution was then pumped into the flask kept at 290 °C with the injection of 20 min using a New Era Pump Systems NE-1000 syringe pump. Then, the mixture was allowed to react at 290 °C for 5 min. Afterward, the flask was left to cool naturally to ambient temperature. Finally, NRs were collected by precipitation, adding 15 mL hexane, and centrifuging the solution at 5500 rpm for 5 min. The supernatant was discarded, and the precipitate was dispersed in 5 mL hexane for further use.

Ligand Exchange: Native organic ligands were displaced from the NRs surface using an NH$_4$SCN solution. Briefly, 1 mL hexane solution containing NRs (5 mg mL^{-1} in hexane) was mixed with 1 mL 0.15 M NH$_4$SCN solution (in ethanol). The mixture was then shacked for several minutes with a vortex and finally centrifuged at 4000 rpm for 3 min. The resulting product was further washed with 2 mL ethanol twice to remove residual NH$_4$SCN.

Material Characterization: The crystal structures of the samples were identified by XRD (a Bruker AXS D8 Advance X-ray diffractometer) using Ni-filtered Cu-Kα irradiation at 45 kV and a diffracted beam monochromator at 40 mA. SEM (Zeiss Auriga) was used to obtain the surface morphology. Elemental analysis was conducted using an Oxford EDX combined with the Zeiss Auriga SEM working at 20.0 kV. The lattice structure of TiO$_2$ was visualized by phase-contrast HRTEM carried out with 300 keV electrons in an FEI Tecnai F20 Field emission instrument. UV–vis diffuse reflectance spectra were obtained by a UV–vis spectrometer (Shimazu) using BaSO$_4$ as the background. XPS experiments were performed using a Physical Electronics VersaProbe III instrument equipped with a monochromatic Al kα x-ray source (hν = 1,486.6 eV) and a concentric hemispherical analyzer. Raman spectroscopy was performed on a Renishaw inVia Qontor confocal Raman microscope using a laser excitation source of 532 nm. EPR measurements were conducted at 9.39 GHz using a Bruker EMXmicro6/1 spectrometer.

Electrochemical Measurements: Electrochemical characterization was performed in a three-electrode system using an electrochemical workstation (CHI760e). A Pt mesh and Ag/AgCl were used as the counter and reference electrodes, respectively. To prepare the working electrode, 2 mg of NRs was dispersed in 2 mL ethanol by sonicating for obtaining a homogeneous ink. The inks were coated onto ITO (2.5 × 4.8 cm^2) substrate and then annealed at 200 °C for 1 h in the glovebox. An active area of 2.5 × 4 cm^2 was left for tests. 1 M LiClO$_4$/PC solution was used as an electrolyte. The electrolyte was purged with Ar for 30 min before the measurement. For EIS measurements, the frequency was swept from 1 to 10 MHz with a sinusoidal amplitude of 5 mV. M–S spectra were obtained by scanning the bias potential from −1.2 to 0.2 V versus Ag/AgCl at a scan rate of 0.01 V s^{-1}, and 0.5 M Na$_2$SO$_4$ solution was used as an electrolyte. The geometric area of the nanorods was calculated taking into account their dimensions, the density of brookite TiO$_2$ (4130 kg m^{-3}), and the amount of TiO$_2$ deposited on the 1 × 2 cm^2 substrate (0.05 mg).

Preparation of TiO$_2$ NRs Thin Film Electrodes: A 5 × 5 cm ITO glass (20 Ω sq^{-1}) was first thoroughly cleaned with acetone solution for 30 min and rinsed with ethanol for another 30 min. 100 μL of the TiO$_2$ NR solution (≈35 mg mL^{-1}) was then spun-coated onto the ITO glass at 500 rpm for 60 s. After drying on a hot plate at 200 °C for 5 min, a second spin-coating was applied. Spin-coating was repeated four times (total spin-coating times is 5). The as-deposited TiO$_2$ NR film on ITO glass was then heated in the air at 350 °C for 45 min to remove the organic ligands.

Preparation of NiLi$_{0.83}$Ti$_{0.28}$O$_x$-Based Counter Electrode: The NiLi$_{0.83}$Ti$_{0.28}$O$_x$-based counter electrode was prepared by the sol-gel spin coating method. The precursor solution was prepared from a mixture of 610 mg Ni(CH$_3$COO)$_2$ 4H$_2$O, 134 mg CH$_3$COOLi, and 200 mg Ti(OC$_3$H$_7$)$_4$ in 10 mL ethanol. The freshly prepared precursor solution was spin-coated on a clean ITO glass at 500 rpm for 60 s. After drying over a hot plate at 200 °C for 5 min, a second layer was spin-coated and dried, and this procedure was repeated four times. The NiLi$_{0.83}$Ti$_{0.28}$O$_x$-coated ITO glass was then annealed in air at 350 °C for 45 min.

Assembly and Measurement of ESW: The ESW device was assembled by using a TiO$_2$ thin film as the cathode, a NiLi$_{0.83}$Ti$_{0.28}$O$_x$-based film as the anode, and a 1 M LiClO$_4$/PC solution as the electrolyte. An active area of 2.5 × 4 cm^2 was left for tests. The two facing electrodes of the optical cell were spaced apart by a ∼1 mm thickness double-sided tape. The electrolyte was introduced into the cell cavity with a syringe and the cell was sealed with double-sided tape. For the 2-electrode device measurements, in situ optical transmission spectra were recorded as a function of the applied voltage on an ocean optics machine (USB2000+XR1-ES). The background transmittance of the ESW device without applied voltage was used as the baseline. Energy input and output (E, Wh m^{-2}) were calculated based on

ADVANCED
SCIENCE NEWS

www.advancedsciencenews.com

NANO · MICRO
small
www.small-journal.com

the equation: $E = \int UIdt$, where U (V) is the voltage, I is the current density (A m^{-2}), and t (h) is the time.

Supporting Information

Supporting Information is available from the Wiley Online Library or from the author.

Acknowledgements

Conflict of Interest

The authors declare no conflict of interest.

Author Contributions

C.X. and L.Y. contributed equally to this work. The manuscript was written through the contributions of all authors. All authors have approved the final version of the manuscript.

Data Availability Statement

The data that support the findings of this study are available in the supplementary material of this article.

Keywords

[1] P. Yang, P. Sun, W. Mai, *Mater. Today* **2016**, *19*, 394.

[2] M. A. F. Nejad, S. Ranjbar, C. Parolo, E. P. Nguyen, R. Álvarez-Diduk, M. R. Hormozi-Nezhad, A. Merkoçi, *Mater. Today* **2021**, *50*, 476.

[3] V. K. Thakur, G. Ding, J. Ma, P. S. Lee, X. Lu, *Adv. Mater.* **2012**, *24*, 4071.

[4] S. Zhang, S. Cao, T. Zhang, A. Fisher, J. Y. Lee, *Energy Environ. Sci.* **2018**, *11*, 2884.

[5] R. J. Mortimer, *Chem. Soc. Rev.* **1997**, *26*, 147.

[6] R. Celiesiute, A. Ramanaviciene, M. Gicevicius, A. Ramanavicius, *Crit. Rev. Anal. Chem.* **2019**, *49*, 195.

[7] M. A. Macedo, L. H. Dall Antonia, B. Valla, M. A. Aegerter, *J. Non-Cryst. Solids* **1992**, *147*, 792.

[8] M. Wang, X. Xing, I. F. Perepichka, Y. Shi, D. Zhou, P. Wu, H. Meng, *Adv. Energy Mater.* **2019**, *9*, 1900433.

[9] G. Yang, Y.-M. Zhang, Y. Cai, B. Yang, C. Gu, S. X.-A. Zhang, *Chem. Soc. Rev.* **2020**, *49*, 8687.

[10] Z. Lu, X. Zhong, X. Liu, J. Wang, X. Diao, *Phys. Chem. Chem. Phys.* **2021**, *23*, 14126.

[11] A. Abdollahi, H. Roghani-Mamaqani, B. Razavi, *Prog. Polym. Sci.* **2019**, *98*, 101149.

[12] S. Yan, K. P. Abhilash, L. Tang, M. Yang, Y. Ma, Q. Xia, Q. Guo, H. Xia, *Small* **2019**, *15*, 1804371.

[13] L. Yu, X. Xing, D. Fang, H. Meng, *Adv. Opt. Mater.* **2022**, *10*, 2201423.

[14] T.-H. Le, Y. Kim, H. Yoon, *Polymers* **2017**, *9*, 150.

[15] Q. Meng, S. Cao, J. Guo, Q. Wang, K. Wang, T. Yang, R. Zeng, J. Zhao, B. Zou, *J. Energy Chem.* **2023**, *77*, 137.

[16] A. Ghicov, H. Tsuchiya, R. Hahn, J. M. Macak, A. G. Muñoz, P. Schmuki, *Electrochem. Commun.* **2006**, *8*, 528.

[17] B. Zhang, H. Wang, Y. Xiang, H. Jiang, L. Tang, J. Luo, Y. Tian, *Electrochim. Acta* **2023**, *440*, 141749.

[18] Z. Liu, J. Yang, G. Leftheriotis, H. Huang, Y. Xia, Y. Gan, W. Zhang, J. Zhang, *Sustainable Mater. Technol.* **2022**, *31*, 00372.

[19] S. Santhosh, K. Balamurugan, M. Mathankumar, K. Shankar, B. Subramanian, *Opt. Mater.* **2023**, *135*, 113248.

[20] G. K. Ong, C. A. Saez Cabezas, M. N. Dominguez, S. L. Skjærvø, S. Heo, D. J. Milliron, *Chem. Mater.* **2019**, *32*, 468.

[21] F. Zhao, Z. Cheng, G. Xu, Y. Liu, G. Han, *Electrochim. Acta* **2023**, *441*, 141863.

[22] K. Xu, L. Wang, S. Xiong, C. Ge, L. Wang, B. Wang, W. Wang, M. Chen, G. Liu, *Electrochim. Acta* **2023**, *441*, 141812.

[23] T. Rao, Y. Zhou, J. Jiang, P. Yang, X. Wang, W. Liao, *J. Electrochem. Soc.* **2022**, *169*, 066506.

[24] A. Arash, S. A. Tawfik, M. J. S. Spencer, S. Kumar Jain, S. Arash, A. Mazumder, E. Mayes, F. Rahman, M. Singh, V. Bansal, *ACS Appl. Mater. Interfaces* **2020**, *12*, 16997.

[25] W. Hu, L. Li, G. Li, Y. Liu, R. L. Withers, *Sci. Rep.* **2014**, *4*, 6582.

[26] N. N. Dinh, N. M. Quyen, M. Zikova, V.-V. Truong, *Sol. Energy Mater. Sol. Cells* **2011**, *95*, 618.

[27] S. Zhang, S. Cao, T. Zhang, J. Y. Lee, *Adv. Mater.* **2020**, *32*, 2004686.[CrossRef]

[28] J. Xiong, A. Fei, L. Yu, L. Xia, C. Xu, S. Chen, G. Jiang, S. Yuan, *Int. J. Electrochem. Sci.* **2021**, *16*, 210542.

[29] B. Zhang, G. Y. Xu, S. J. Tan, C. Y. Liu, J. C. Zhang, *Opt. Mater.* **2020**, *100*, 109659.

[30] C. Dong, A. Li, L. Zhang, W. Dong, H. Gao, X. Jia, X. Chen, H. Mi, G. Wang, X.-B. Chen, *J. Power Sources* **2020**, *448*, 227458.

[31] R. A. Patil, R. S. Devan, Y. Liou, Y. R. Ma, *Sol. Energy Mater. Sol. Cells* **2016**, *147*, 240.

[32] M. K. Singh, M. S. Mehata, *Optik* **2019**, *193*, 163011.

[33] D. Dambournet, I. Belharouak, K. Amine, *Chem. Mater.* **2010**, *22*, 1173.

[34] T. Mizoguchi, I. Tanaka, S. Yoshioka, M. Kunisu, T. Yamamoto, W. Y. Ching, *Phys. Rev. B* **2004**, *70*, 045103.

[35] X. Wang, J. Li, Q. Xue, X. Han, C. Xing, Z. Liang, P. Guardia, Y. Zuo, R. Du, L. Balcells, J. Arbiol, J. Llorca, X. Qi, A. Cabot, *ACS Nano* **2023**, *17*, 825.

[36] R. Du, K. Xiao, B. Li, X. Han, C. Zhang, X. Wang, Y. Zuo, P. Guardia, J. Li, J. Chen, J. Arbiol, A. Cabot, *Chem. Eng. J.* **2022**, *441*, 135999.

[37] X. Wang, X. Han, R. Du, Z. Liang, Y. Zuo, P. Guardia, J. Li, J. Llorca, J. Arbiol, R. Zheng, A. Cabot, *Appl. Catal., B* **2023**, *320*, 121988.

[38] T. Berestok, J. Jesús Chacón-Borrero, J. Li, P. Guardia, A. Cabot, *Langmuir* **2023**, *39*, 3692.

[39] G. Montaña-Mora, X. Qi, X. Wang, J. Chacón-Borrero, P. R. Martinez-Alanis, X. Yu, J. Li, Q. Xue, J. Arbiol, M. Ibáñez, A. Cabot, *J. Electroanal. Chem.* **2023**, *936*, 117369.

[40] J. Dai, C. Yang, Y. Xu, X. Wang, S. Yang, D. Li, L. Luo, L. Xia, J. Li, X. Qi, *Adv. Mater.* **2023**, 2303732. [CrossRef]

[41] R. He, L. Yang, Y. Zhang, X. Wang, S. Lee, T. Zhang, L. Li, Z. Liang, J. Chen, J. Li, *Energy Storage Mater.* **2023**, *58*, 287.

[42] R. C. Pullar, R. Giannuzzi, T. Prontera, D. M. Tobaldi, M. Pugliese, L. De Marco, P. Cossari, G. Gigli, V. Maiorano, *Energy Adv.* **2022**, *1*, 321.

[43] J. Cai, D. Yu, Y. Zhang, S. Yao, X. Zhang, J. Cui, Y. Wang, J. Liu, C. Yu, X. Sun, *J. Electroanal. Chem.* **2022**, *914*, 116304.

[44] P. Shao, S. Huang, B. Li, Q. Huang, Y. Zhang, R.-T. Wen, *Mater. Today Phys.* **2023**, *30*, 100958.

[45] S. Huang, R. Zhang, P. Shao, Y. Zhang, R. Wen, *Adv. Opt. Mater.* **2022**, *10*, 2200903.

[46] R.-T. Wen, G. A. Niklasson, C. G. Granqvist, *ACS Appl. Mater. Interfaces* **2016**, *8*, 5777.

[47] H. P. Zhang, Y. Lei, *Adv. Energy Mater.* **2020**, *10*, 2001460.

[48] L. Liang, Y. Xu, C. Wang, L. Wen, Y. Fang, Y. Mi, M. Zhou, H. Zhao, Y. Lei, *Energy Environ. Sci.* **2015**, *8*, 2954.

[49] J.-Z. Chen, W.-Y. Ko, Y.-C. Yen, P.-H. Chen, K.-J. Lin, *ACS Nano* **2012**, *6*, 6633.

[50] Y. Chen, X. Li, Z. Bi, X. He, X. Xu, X. Gao, *Electrochim. Acta* **2017**, *251*, 546.

[51] X. Che, L. Li, J. Zheng, G. Li, Q. Shi, *J. Chem. Thermodyn.* **2016**, *93*, 45.

[52] N. Roy, Y. Sohn, D. Pradhan, *ACS Nano* **2013**, *7*, 2532.

[53] D. N. Pei, L. Gong, A. Y. Zhang, X. Zhang, J. J. Chen, Y. Mu, H. Q. Yu, *Nat. Commun.* **2015**, *6*, 8696.

[54] A. John, J. Naduvath, S. Mallick, T. Shripathi, M. Thankamoniamma, R. R. Philip, *Nanoscale* **2015**, *7*, 20386.

[55] D. D. Qin, Y. P. Bi, X. J. Feng, W. Wang, G. D. Barber, T. Wang, Y. M. Song, X. Q. Lu, T. E. Mallouk, *Chem. Mater.* **2015**, *27*, 4180.

[56] M. Cargnello, T. Montini, S. Y. Smolin, J. B. Priebe, J. J. Delgado Jaen, V. V. Doan-Nguyen, V. V. McKay, J. A. Schwalbe, M. M. Pohl, T. R. Gordon, Y. Lu, J. B. Baxter, A. Bruckner, P. Fornasiero, C. B. Murray, *Proc. Natl. Acad. Sci. U. S. A.* **2016**, *113*, 3966.

[57] G. A. Tompsett, G. A. Bowmaker, R. P. Cooney, J. B. Metson, K. A. Rodgers, J. M. Seakins, *J. Raman Spectrosc.* **1995**, *26*, 57.

[58] C. Y. Lu, Y. Y. Ma, Y. Cao, Q. G. Huang, J. L. Wang, *Chem. Eng. J.* **2023**, *468*, 143598.

[59] C. S. He, L. L. Yang, X. H. Peng, S. H. Liu, J. Wang, C. Y. Dong, D. L. Du, L. G. Li, L. Z. Bu, X. Q. Huang, *ACS Nano* **2023**, *17*, 5861.

[60] D. L. Liang, Z. Y. Guo, Y. Z. Su, F. Zhou, M. Wang, W. N. Chen, G. Zhou, *Adv. Mater. Technol.* **2023**, 2300454.

[61] B. Seelandt, M. Wark, *Microporous Mesoporous Mater.* **2012**, *164*, 67.

[62] C. Eyovge, C. S. Deenen, F. Ruiz-Zepeda, S. Bartling, Y. Smirnov, M. Morales-Masis, A. Susarrey-Arce, H. Gardeniers, *ACS Appl. Nano Mater.* **2021**, *4*, 8600.

[63] K. Wang, Q. Meng, Q. Wang, W. Zhang, J. Guo, S. Cao, A. Y. Elezzabi, W. W. Yu, L. Liu, H. Li, *Adv. Sustainable Syst.* **2021**, *2*, 2100117.

[64] S. Cao, S. Zhang, T. Zhang, Q. Yao, J. Y. Lee, *Joule* **2019**, *3*, 1152.

[65] J. Zhang, J. Yang, G. Leftheriotis, H. Huang, Y. Xia, C. Liang, Y. Gan, W. Zhang, *Electrochim. Acta* **2020**, *345*, 136235.

[66] K. Wang, H. Wu, Y. Meng, Y. Zhang, Z. Wei, *Energy Environ. Sci.* **2012**, *5*, 8384.

[67] H.-C. Lu, B. Z. Zydlewski, B. Tandon, S. A. Shubert-Zuleta, D. J. Milliron, *Chem. Mater.* **2022**, *34*, 5621.

[68] G. Garcia, R. Buonsanti, E. L. Runnerstrom, R. J. Mendelsberg, A. Llordes, A. Anders, T. J. Richardson, D. J. Milliron, *Nano Lett.* **2011**, *11*, 4415.

2303639 (11 of 11)